# Parallel computing for modeling multilayer photonic crystals

**Andreas T. D. Richardson**,[a] **Shavaiz I. Mir**,[a] **Stephen M. Morris**,[b] **Steve J. Elston**,[b] **Ali K. Yetisen**,[a] **and Yunuen Montelongo**[b,*]

[a]Imperial College London, Department of Chemical Engineering, London, United Kingdom
[b]University of Oxford, Department of Engineering Science, Oxford, United Kingdom

**Abstract.** A simulation framework is developed for the two-dimensional finite-difference time-domain to model multilayer photonic crystal structures. The framework includes the recording process in a photosensitive material through a coherent light source and then a subsequent interrogation with a broadband spectrum. Moreover, the tunable response of the photonic crystal is simulated for different film thicknesses (recorded from 5 to 20 $\mu$m), refractive indices contrast (ranging from 4% to 24%), film expansions (interrogated with expansions ranging 110% to 160%), and lattice spacings (recorded with wavelengths from 360 to 560 nm). A parallelization method was implemented in a computer cluster to alleviate the required high computational demand. Through this simulation framework, it is now possible to retrieve relevant information about realistic photosensitive multilayer structures. This method will support the design of multilayer structures utilized in sensors, lasers, and other functional nanostructured photonic devices. © *2023 Society of Photo-Optical Instrumentation Engineers (SPIE)* [DOI: 10.1117/1.JNP.17.016007]

**Keywords:** simulations; finite-difference time-domain; photonic crystals; parallel computation.

Paper 22123L received Nov. 21, 2022; accepted for publication Jan. 26, 2023; published online Feb. 18, 2023.

## 1 Introduction

Functional multilayer photonic crystals have become the basis of numerous applications including light filtering,[1] structured light pigments,[2] tunable lasers,[3] and sensors.[4] Photonic crystal-based sensors have become a particular area of interest due to their capability to manipulate multiple properties of light by responding to chemical and physical stimuli.[5] The rise of the "quantified-self" movement[6] has seen the integration of such sensors in wearable devices with applications such as the monitoring of biomarkers, but also in other areas such as rewritable photonic materials, pharmaceutical bioassays, medical diagnostics, and food and water quality control.[7]

In terms of the fabrication of these photonic crystal-based sensors, laser-induced photochemical patterning offers a cost-effective method to fabricate holographic sensors that can be used to form periodic, multilayered polymer structures in photosensitive materials.[8,9] Moreover, the introduction of porous materials, such as hydrogels, provides the opportunity for tuning the color-selective diffracted signal. Toward this end, recent progress in nanofabrication has unlocked possibilities to create such porous nanostructured materials for sensing applications.[10] In this method, two polymers are employed to create a multilayer photonic crystal. First, a backbone porous polymer (referred to in this text as backbone material) is crosslinked with incoherent ultraviolet (UV) light. Second, another photosensitive material (referred to as lattice material) is selectively crosslinked with the aid of the interference of two UV laser beams. In the case of two counter-propagating beams, selective polymerisation occurs at the antinodes, forming a multilayer structure of alternating layers of backbone material and a lattice material with a spacing of a half wavelength. These nanostructured porous materials have the ability to change thickness reversibly by absorbing a fluid through a Donnan osmotic

*Address all correspondence to Yunuen Montelongo, yunuen.montelongo@eng.ox.ac.uk

1934-2608/2023/$28.00 © 2023 SPIE



Downloaded From: https://www.spiedigitallibrary.org/journals/Journal-of-Nanophotonics on 09 May 2023
Terms of Use: https://www.spiedigitallibrary.org/terms-of-use

pressure.[11,12] This in turn alters the periodicity, shifting the narrow band diffraction peak toward longer wavelengths. The swelling of the film during exposure directly influences the spectral replay bandwidth, allowing for the tunability of the wavelength that the sensor operates across. To a first approximation, the diffraction wavelength obeys Bragg's law; however, the diffraction is produced by two interlacing materials of different refractive indices. The modeling of these materials complicates the situation even further when considering that the refractive indices change while the material expands. Accurately modeling the response of these nanostructured materials requires sophisticated numerical simulations.

Various modeling methods have been developed to simulate the optical properties of photonic crystals. Common methods include analytical approaches such as the plane wave expansion method as well as numerical methods such as the finite element (FE), finite-difference time-domain (FDTD), and boundary element methods.[13–16] The plane wave method is often used to simulate photonic crystals with frequency-independent permittivity and permeability. Photonic crystals are modeled in the Fourier domain.[13] In Fourier space, Maxwell's equations can be expressed in terms of Helmholtz's equation, forming a standard eigenvalue problem that can be solved. A similar method was utilized to retrieve the multilayer of crystal structure recorded by interfering laser beams.[17]

Progress has been made for the full numerical calculation of light propagation in Bragg stacks. For nanoparticle-hydrogel gratings, the FE method has been utilized to simulate the effect of particle size, number of stacks, lattice spacing, and defects.[5,6,18] On the other hand, the FDTD method is one of the most common numerical tools employed to solve problems involving the propagation of EM waves. The FDTD method has the advantage of maintaining robustness without sacrificing efficiency.[19] The method works by discretizing and computing the electric and magnetic fields through Maxwell equations in a square grid. Through these numerical calculations, the EM wave propagates in both time and space. For each time/space increment, updated equations are formulated using central difference approximations and are used to calculate the fields in the next time step from the previously calculated steps. An iteration in which electric and magnetic fields are successively calculated in turns is therefore created and can continue until the desired time length is achieved.[15] Although this method has been successfully utilized to model complex crystal structures, it requires calculations for each spatial unit for each time step. This calculation process can be extremely large when modeling over practical length scales. In particular, multiple simulations for independent wavelengths can become computationally expensive. As an example, a two-dimensional grid spaced in 100 nm increments requires the calculation of one million spatial units to simulate a square of $100 \times 100$ $\mu$m for every time step. This calculated in today's high-performance personal computers (e.g., AMD Ryzen 9 5980HS) takes 50 milliseconds per time step. At least 1000 cycles are required to start obtaining reliable results; however, 10,000 are desired for higher accuracy. This becomes complicated when independent simulations are performed for different wavelengths and multiple conditions and devices are compared. Although broadband simulations can reduce the time for multiple wavelengths, high accuracy is only reached by averaging long timespans. Different strategies have been implemented to increase the speed and accuracy of FDTD simulations. For instance, machine learning-based algorithms have acquired relevance in recent years.[20,21] Perfectly matched layers and nanoplasmonics have been implemented with neural networks.[22,23] More importantly, the parallelization of the process has become a fundamental tool for the acceleration of the FDTD calculation.[24–26] Parallelization has shown successful results with dielectrics and plasmonic elements.[27]

Here we present a strategy to numerically calculate multiple parameters simultaneously using parallelization. A computational algorithm based on the FDTD method is implemented in MATLAB and then parallelized in multiple processing units. First, the recording process is simulated through the local polymerization produced by two counter-propagating coherent beams. Then the obtained recorded material is utilized to define the spatial modulation of the refractive indices through the material. The reading process is executed in multiple processing units to obtain the resulting diffraction properties for different wavelengths and different film parameters. Through this approach, the numerical simulation process is accelerated, allowing for the possibility of testing practically realizable geometries and comparing different parameters and rapid time scales.



Downloaded From: https://www.spiedigitallibrary.org/journals/Journal-of-Nanophotonics on 09 May 2023
Terms of Use: https://www.spiedigitallibrary.org/terms-of-use

## 2 Modeling Framework

The ultimate goal of the simulation framework presented here is to correlate the EM behavior and mechanical response of a multilayer photonic crystal. We simulated the optical response of four different experiments for multilayer crystals recorded with counter-propagating coherent beams. These simulations are employed to retrieve the wavelength response and intensity peak as a function of lattice spacing, refractive index contrast, film width, and film expansion.

Herein, we focus on the implementation of an FDTD algorithm, also known as Yee's method.[15] This method consists of simulating the time evolution of propagating EM waves through the numerical solution of equations that form the basis of Ampere's law and Faraday's law. The method described by Yee solves Ampere's equation and Faraday's equation by discretizing the electrical and magnetic fields in space and time. In the Yee algorithm, the equations are iteratively updated, allowing for the evaluation of the electric and magnetic fields at consecutive time steps. The combination of these processes results in the time evolution of the system, whereby the electric and magnetic fields are successively retrieved for a given time length. The fields are additionally offset from each other in space and time, allowing for the use of central difference approximations to the derivatives. Alternatively, the derivatives can be replaced with their Fourier domain representation for higher accuracy. In this context, the pseudospectral time domain finite difference time domain (PSTD FDTD) method is a better alternative for parallelization. In particular, a PSTD FDTD method was implemented due to its high accuracy. It has been shown that this method can reach reliable results when the spatial sampling is higher than five times the size of the propagated wavelength.[28] Negligible inconsistencies were observed compared with the Mie analytical solutions for the EM scattering of particles.

The general approach used to model our system requires both writing the procedure to form the photonic crystal structure by interfering with coherent beams and interrogating the structure at multiple wavelengths. It should be noted that the process of writing the samples is not as computationally expensive as the process of reading the sample. The writing process imitates the action of a monochromatic source, and hence, the radiation is emitted with the oscillation of the source at one single frequency. Once the structure is formed through the writing process, the reading simulation takes place. In contrast to the writing simulation, the reading process requires multiple independent simulations for each tested wavelength. To form the full spectrum, each wavelength is tested through different oscillation frequencies emitted from the source.

### 2.1 *Designing the Photonic Crystal Sensor*

The full simulation sequence required to retrieve a measurement is similar to the actual experimental process [Fig. 1(a)]. First, a source, a material, and a mirror are designed within a graphic editor. Next, the material is recorded with a simulation of the writing procedure. Third, the material is characterized by multiple wavelengths. Finally, the diffraction efficiency is retrieved from the propagated EM wave. A strategy in which multiple reading wavelengths are computed in parallel is implemented through a computer cluster [Fig. 1(b)]. Depending on the simulation, we utilized between 10 and 20 independent processing units with multiple threads. Through this strategy, we reached up to 50 times the speed observed in a personal computer. This acceleration opened the possibility of analyzing the full spectral response and the effects of particular physical conditions of the diffractive elements.

### 2.2 *Write Process*

Object bitmaps, including a planar source, a mirror, and a tilted film at 5 deg, were created to define the permittivity at each point [Fig. 2(a)]. The permittivity inside the photosensitive medium is defined by the refractive index of a backbone material (1.37). The background was set to air, and the permeability was assumed to be the vacuum everywhere. The film was assumed to have a uniform permittivity that was extracted from the refractive index of the material. A coherent recording oscillation was defined at the source, which allowed the wave to traverse the medium and film, before being reflected in the mirror. The oscillation duration was sufficient



Downloaded From: https://www.spiedigitallibrary.org/journals/Journal-of-Nanophotonics on 09 May 2023
Terms of Use: https://www.spiedigitallibrary.org/terms-of-use

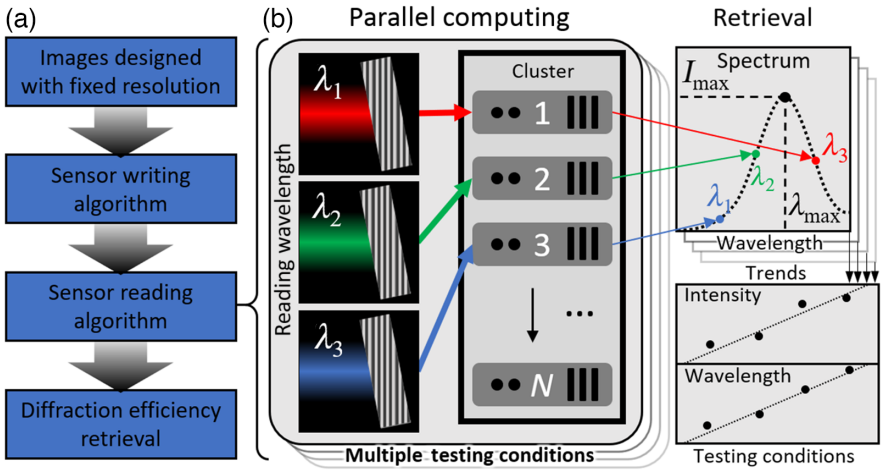



**Fig. 1** Overview of the computational simulation strategy: (a) flowchart describing the four stages for the simulation of the photonic crystal sensors, starting with the design of the materials in a bit map format, then the writing process and the reading of the sensor, and finally the retrieval of the diffraction efficiencies. (b) Expansion of the reading process for different wavelengths. The simulations of different wavelengths are executed in parallel through a computer cluster. Then the intensities retrieved for each wavelength are merged to reconstruct the full spectral response. Finally, the intensity and wavelength peaks are retrieved to visualize the trends under different conditions.

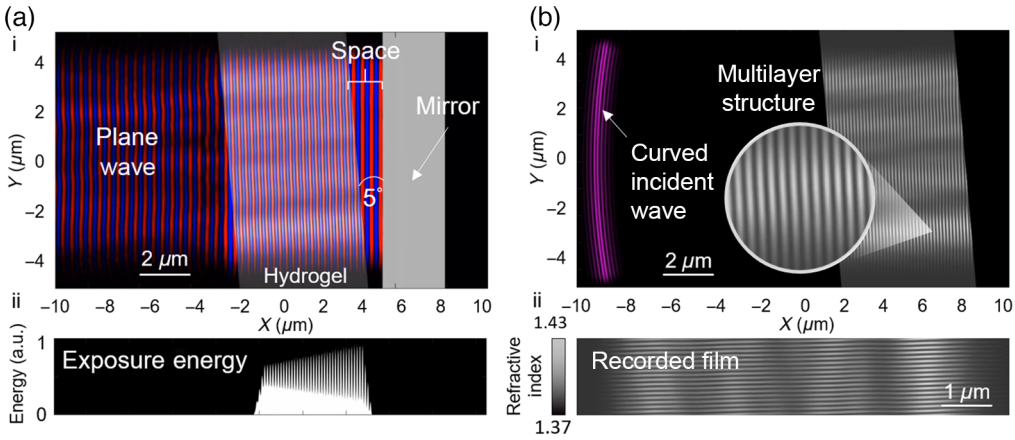



**Fig. 2** Simulation illustrations of the writing process for the multilayer photonic crystal and the subsequent read process. (a) (i) Screenshot of an example simulation of wave propagation through a hydrogel matrix with a 360-nm beam to form the photonic crystal sensor. (ii) Exposure energy distribution throughout the writing process (horizontal coordinates correspond with the hydrogel in the top panel). (b) (i) Screenshot of an example simulation of the reading process using a curved wavefront. (ii) Multilayer crystal structure recorded during the writing process and introduced for the reading process.

to cause the incident and reflected wave to coincide within the film. The emitted EM wave interferes with the reflected wave from the mirror, forming a standing wave. The maximum intensity is formed at the antinodes of the standing wave, and the destructive interference vanishes at the nodes. Therefore, the constructive interference selectively sensitizes the material to produce a multilayer structure. To simulate this process, at each time step, the intensity of the electric field was measured and summed, representing the total radiant exposure of the material. As a first approach, the normalized light intensity at each point in the photosensitive material can be linearly correlated to the refractive index, but a more precise representation of the correlation can include other factors. For instance, reaction-diffusion kinetics solved in MATLAB has been



Downloaded From: https://www.spiedigitallibrary.org/journals/Journal-of-Nanophotonics on 09 May 2023
Terms of Use: https://www.spiedigitallibrary.org/terms-of-use

demonstrated for a UV-curable resin.[29] Furthermore, the addition of thermomechanical modeling to the chemical kinetics permits the characterization of thermal expansion and chemical shrinkage of the cured polymer.[30] A further enhancement of the model quality is to consider the inherent stochasticity of the photopolymerization approach.[31] Herein, we utilized linear correlations between the exposure of the material and the resulting refractive index. The final exposure film matrix was recorded as an image that which in turn was linked with the change in refractive index. The exposure matrix was then passed as material for the reading stage [Fig. 2(b)].

### 2.3 *Read Process*

Porous polymeric matrices have technological interest due to their resilience and capability to physically change under external stimuli. Here we study the optical effects produced by physical changes of multilayer polymeric matrices. To reach this objective, the structures recorded during the writing stage were loaded and then linearly transformed to emulate the expansion or the contraction [Fig. 2(b)]. The refractive index (and hence, permittivity) at each point in the film was defined by interpolating between the values for the backbone and the lattice materials according to the relative intensity recorded at each point in the simulation of the writing process.[10]

The background was set to water to emulate the use of the physical sensor in an aqueous solution. The source was modeled to a curved wavefront to resemble the focus of the incoming beam on the center of the film. The diffraction efficiency was retrieved from the completed simulations.

It should be noted that, as the thickness of the film expanded, the resolution of the image increased (to keep the size of each pixel constant). For instance, doubling the size of the film resulted in a factor of 4 in the computation time. Here increasing the size of the film from 5 to 20 $\mu$m requires a run time of 16× longer. The large number of runs required to observe relationships and trends is a constraint that increases in complexity exponentially. To alleviate this problem, we designed a strategy to compute in parallel the behavior for multiple wavelengths simultaneously [Fig. 1(b)].

Once the simulations ended, the measurement of the diffraction intensity for each wavelength was executed. To retrieve the diffraction efficiency for each wavelength, it was necessary to define a measurement region where all of the diffracted light was measured. The intensity was obtained by adding the electric field in each pixel inside the measurement region. The measured intensity is then the square of this electric field. Similarly, a reference measurement of the incoming intensity was obtained with a virtual sensor at the output of the source. Then the diffraction efficiency was calculated as the ratio of the intensity of the diffracted wave to that of the input wave. Finally, the spectral responses and the peak trends were collected and plotted.

Four different types of simulations were carried out to retrieve the spectral response and intensity peaks for a range of different parameters. Specifically, these simulations correspond to changes in the film thickness, refractive index contrast, film expansion, and lattice spacing of the photonic crystal. The simulations and results are described in the following section.

## 3 Simulation Results

### 3.1 *Film Thickness*

A series of simulations for different film thicknesses (5, 6, 8, 10, 15, and 20 $\mu$m) were computed [Fig. 3(a)]. The refractive indices in the film were defined as 1.37 for the backbone material and 1.65 for the lattice material. To maintain a 20-nm pixel pitch, to satisfy the Nyquist–Shannon sampling criterion,[32] it was necessary to expand the simulation grid, which introduced a corresponding increase in the computational cost.

An increase in the diffraction peak is observed due to the increment in the number of diffractive layers [Fig. 3(b)]. A slight decrement in the pattern is observed at 10 $\mu$m due to the resonant ghost effects produced by the Fabry–Perot interference. Also the width of the peak



Downloaded From: https://www.spiedigitallibrary.org/journals/Journal-of-Nanophotonics on 09 May 2023
Terms of Use: https://www.spiedigitallibrary.org/terms-of-use

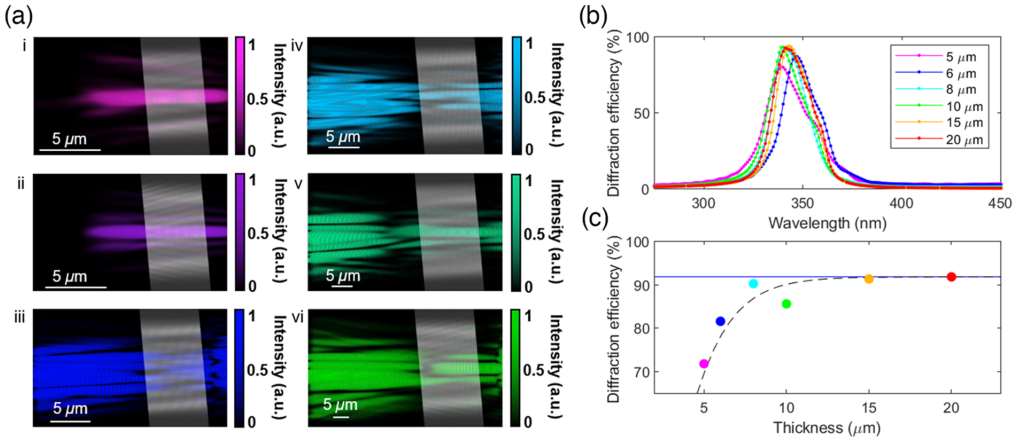



**Fig. 3** Simulation results for varying film thicknesses for photonic crystals written with a 360-nm illumination source. The lattice material refractive index was kept at 1.65. (a) Simulations of the diffracted light through the photonic crystals for the film thickness of (i) 5, (ii) 6, (iii) 8, (iv) 10, (v) 15, and (vi) 20 $\mu$m. The simulations show the diffraction at the peak wavelength. A lower intensity in the diffraction is observed for thinner films, particularly for 5 and 6 $\mu$m. (b) Spectral response obtained from films with different film thicknesses. (c) Plot of the diffraction efficiencies as a function of film thickness. The data were fitted with a hyperbolic tangent from a multilayer model. The blue line is the retrieved specular reflection of 8.2%.

narrows as the film thickness increases. The saturation trend observed in the film is very similar to a multilayer stack. The analytical solution for the diffraction efficiency $\eta$ corresponds to a hyperbolic tangent of the following form:[7]

$$\eta = \tanh^2\left(\pi \frac{\Delta n\, d}{\lambda}\right), \tag{1}$$

where $\Delta n$, $d$, and $\lambda$ are the difference in refractive indices between the backbone and the lattice material, the thickness of the film, and the wavelength, respectively. From this approximation, we fit a curve to the data [Fig. 3(c)] and retrieve the effective difference in the refractive index. We can observe that this difference in effective refractive indices between the backbone and lattice materials is about 3 times less than that expected for a multilayer photonic crystal. This is an important observation as the recorded pattern is not in the form of a square gradient, but instead it forms a superposition of waves. Also it is important to note that the trend does not reach 100% as expected in the multilayer model. The reason for this is the appearance of specular reflection produced when the read beam approaches the film. It can be observed from the fitting of the hyperbolic tangent function that the maximum diffraction efficiency at infinity reaches 91.8%.

Another relevant observation found during this simulation is a minimal change in the peak width of the spectra for different film thicknesses. All of the FWHM values of the peaks are $23 \pm 1.5$ nm except for the thinner with a width of 5 nm where a noticeable expansion of 30 nm is observed. To understand the relation between the film thickness $L$ and the width $\Delta\lambda$ of the spectrum, we utilize the fiber Bragg grating approximation as[33]

$$L = \frac{\lambda}{\Delta n \sqrt{1 - \left(\frac{n}{\lambda}\frac{\Delta\lambda}{\Delta n}\right)^2}}. \tag{2}$$

By applying this approximation, we retrieve a film thickness of 1.57 $\mu$m, which is smaller than the thicknesses simulated. Although this approximation is an analytical expression for a perfect multilayer pattern, it provides an estimation of the penetration length of the beam through the film. This observation is confirmed in a further simulation testing different refractive indices contrast (in the following section).



Downloaded From: https://www.spiedigitallibrary.org/journals/Journal-of-Nanophotonics on 09 May 2023
Terms of Use: https://www.spiedigitallibrary.org/terms-of-use

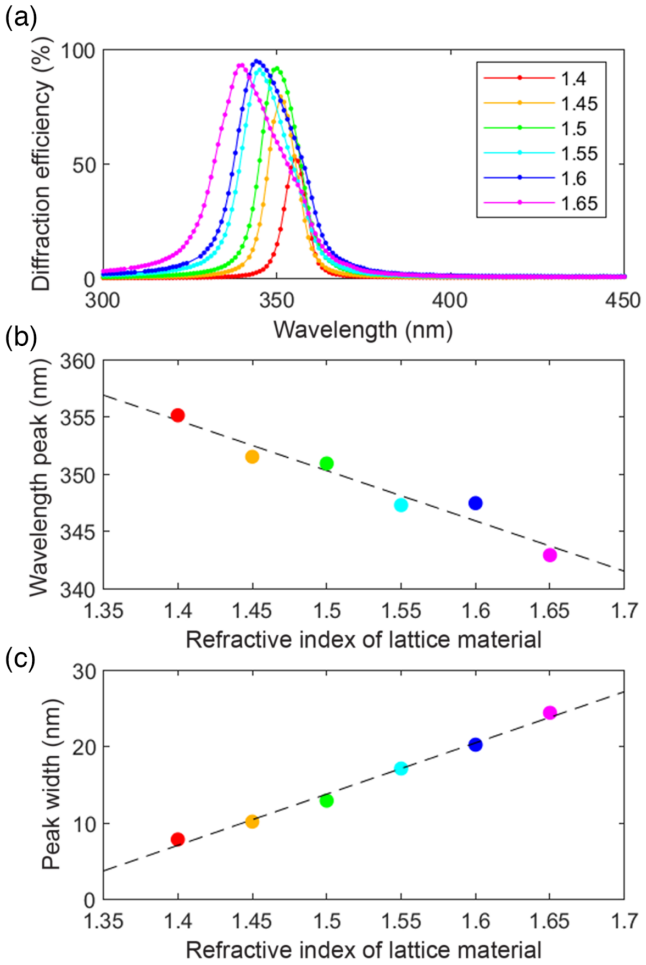



**Fig. 4** Simulation results when the refractive index of the lattice material is varied for a 10-$\mu$m thick film photonic crystal written using a 360-nm illumination source. (a) Spectral response obtained for different lattice material refractive indices (1.65, 1.60, 1.55, 1.50, 1.45, and 1.40). (b) Plot of the peak wavelength as a function of the refractive index of the lattice material. (c) Plot of the peak width as a function of the refractive index of the lattice material.

## 3.2 *Refractive Index Contrast*

A series of multilayer crystal structures were written for films with different refractive indices in the lattice materials (ranging from 1.4 to 1.65 in 0.5 steps), with the backbone material refractive index being kept at 1.37. The effect of the dispersion was minimal in the simulations performed. For instance, in the case of typical plastics utilized in optics, such as PMMA, the change of refractive index is on the order of 0.05 $\mu m^{-1}$ in the optical regime.[34] Therefore, the dispersion was ignored and each simulation was performed with a constant refractive index for all wavelengths. The film thickness remained at 10 $\mu$m for all simulations, and the spatial resolution was maintained at 20 nm. The reading process was executed simultaneously in the computer cluster to obtain the spectral response [Fig. 4(a)]. The increase in the effective refractive index of the combined backbone and lattice materials in the film blueshifted the diffraction peak [Fig. 4(b)]. The blueshift is due to the effective refractive index increase, creating a shrinking of the propagated wave.

As discussed in the previous section, a broadening of the peak is expected with the increment of the refractive index. This effect is produced due to the different penetration lengths of the light beam into the material. At a higher refractive index, contrast more reflection is observed from the first layers of the photonic structure. Following Eq. (2), we can infer an estimated penetration length of the field. Hence we obtain a field penetration of 1.4 $\mu$m for 1.65, 1.8 $\mu$m for 1.6, 2.6 $\mu$m for 1.55, and 5.6 $\mu$m for 1.50. However, after this value, the penetration length is larger



Downloaded From: https://www.spiedigitallibrary.org/journals/Journal-of-Nanophotonics on 09 May 2023
Terms of Use: https://www.spiedigitallibrary.org/terms-of-use

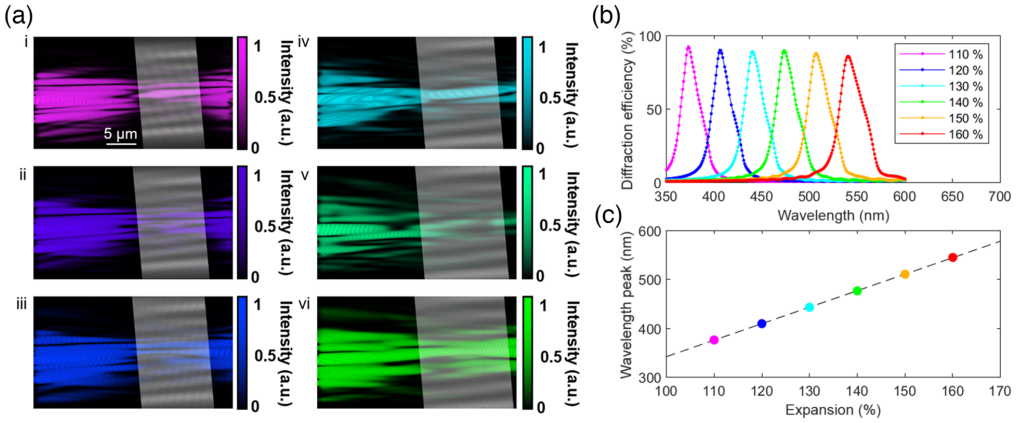



**Fig. 5** Simulation results for six different expansions of a 10-$\mu$m-thick film written with a 360-nm illumination source. The lattice material refractive index was kept at 1.65. (a) Simulations of the diffraction of light through the photonic crystals extended by (i) 110%, (ii) 120%, (iii) 130%, (iv) 140%, (v) 150%, and (vi) 160%. The simulations show the diffracted beam observed at the peak wavelength for each expansion tested. The diffracted beam is observed on the left side of the hydrogel, and the transmitted beam is on the right side. (b) Spectral response obtained from films with different expansions. (c) Plot of the peak wavelength as a function of the expansion of the photonic crystal film. The dashed line represents a linear fit to the data.

than the film thickness, and Eq. (2) shows imaginary numbers. It should be highlighted that this equation is designed for long fiber gratings diffracting most of the light. In this case, the film width is relatively small compared with the penetration of the electromagnetic wave, producing a deformation in the spectral profile. Indeed, the deformation is evident in the spectra [see Fig. 4(a)] for the refractive indices in the lattice materials of 1.4 and 1.45, which correspond to the imaginary region.

### 3.3 *Film Expansion*

Six spectral responses of a 10-$\mu$m thick film that expanded from 110% to 160% of its original size are presented in Fig. 5(a). The film was extended through a linear interpolation of the image matrices with the pixel pitch maintained at 20 nm. The refractive indices in the film were defined as 1.37 for the backbone material and 1.65 for the lattice material. The read processes were executed simultaneously in the computer cluster to obtain the spectral response [Fig. 5(b)].

A clear linear trend was observed in the value of the diffraction peak, highlighting the suitability of the photonic crystal expansion mechanism for sensing [Fig. 5(c)]. Peak diffraction efficiencies were 90% with a slight decrease (5% of variation) for the most expanded films. The wavelength shifts from a diffraction peak at 375 to 540 nm over the investigated range. No clear broadening of the peak was observed in the simulations. The refractive index contrast was maintained as a constant, and most light was reflected.

### 3.4 *Lattice Spacing*

Six different crystal structures were recorded in films with wavelengths ranging from 360 to 560 nm (with a spacing of 40 nm and a spatial resolution of 20 nm). The lattice spacings were obtained by considering $\lambda n/2$ (where $\lambda n$ is the wavelength in the medium), corresponding to 131, 145, 160, 175, 189, and 204 nm. Considering these lattice spacings, the sensitized and backbone interlacing layers have roughly half of these sizes in their thickness. The refractive indices in the film were defined as 1.37 for the backbone material and 1.65 for the lattice material for all wavelengths. The diffraction response at the peak wavelength is shown in Fig. 6(a). The light beam crossing through the material can be observed in each panel. Furthermore, a beam diffracted back is shown on the left side of the hydrogel. Different colors representing different wavelengths were utilized to perceive the diffraction peak for each simulation. Once the



Downloaded From: https://www.spiedigitallibrary.org/journals/Journal-of-Nanophotonics on 09 May 2023
Terms of Use: https://www.spiedigitallibrary.org/terms-of-use

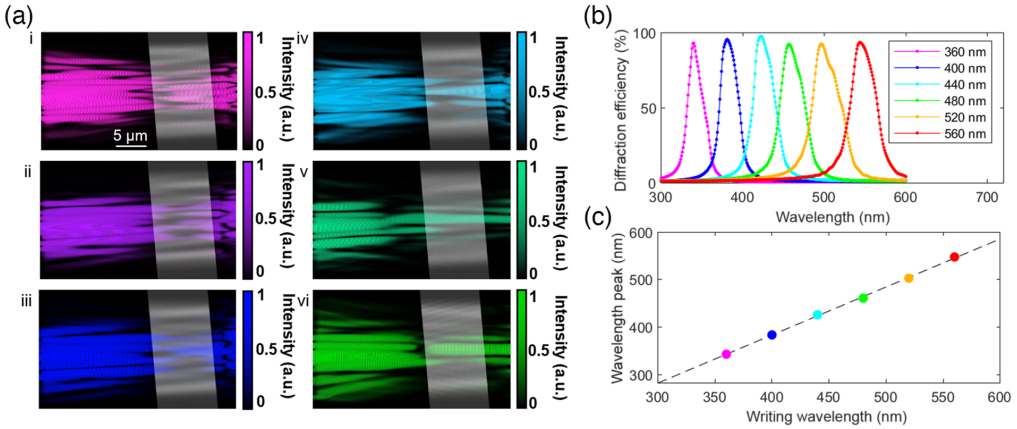



**Fig. 6** Simulation results for varying the lattice spacing of a photonic crystal written in a 10-$\mu$m thick film with a lattice material refractive index of 1.65 for all wavelengths. (a) Simulations of the diffraction of light through photonic crystals written at (i) 360 nm, (ii) 400 nm, (iii) 440 nm, (iv) 480 nm, (v) 520 nm, and (vi) 560 nm. Each panel shows the diffracted beam at the peak wavelength. On the left side of the hydrogel, the diffracted beam is observed; on the right side of the panel, a portion of the undiffracted beam is transmitted. (b) Spectral response obtained from films with different lattice spacings. (c) Plot of the peak wavelength of the diffracted beam as a function of the write wavelength. The dashed line shows a linear fit to the data. The wavelength peak at reading shows a small mismatch compared with the writing wavelength because of the change in refractive indices after exposure.

multilayer pattern was retrieved in the writing simulation, the reading process was executed in parallel on the computer cluster to obtain the spectral responses [Fig. 6(b)].

A strong linear relationship, which follows Bragg's law, can be observed in Fig. 6(c). The simulation shows a redshift in the diffraction peak as the lattice spacing increases. The results also show a rise in the peak width as the lattice spacing increases. It should be noted that the film width is fixed, and hence, the total fringe number embedded in the film increases as the lattice spacing decreases. An important observation is that the wavelength used to read the photonic crystal is not equivalent to the writing wavelength. The reason is that after exposure there is a change in the refractive index in the lattice material. This mismatch in the refractive index also creates a mismatch between the diffraction peak and the writing conditions with a factor of 0.96. Another important observation is that the diffraction intensity does not show a noticeable trend for longer writing wavelengths. Nonetheless, the number of lattices is still relatively large for all tested cases, and it may be necessary to have even larger wavelengths to notice a reduction in the diffraction intensity.

## 4 Conclusion

A method was presented to simulate the writing of multilayer structures and to retrieve their spectral response for different wavelengths. The recorded structures created with this method are comparable to the real recording of photosensitive materials. Inhomogeneities were observed in the recorded thick film due to ghosting effects and multiple modes created by the standing waves. Consequently, the spectral response of the diffraction of these multilayer slanted structures showed complex behaviors compared with the theoretical "Gaussian" or "sinc" functions. In this context, the effects of lattice spacing, refractive indices, film thicknesses, and film expansions were simulated with an FDTD method implemented in a computer cluster. Various geometries were simulated by applying a linear scaling approximation. During the reading process, we identified that the diffraction efficiency increased with the lattice material refractive index and film width. We observed that the peak broadened with an increase in the lattice spacing, lattice material refractive index, and film expansion. The diffraction peak was found to be redshifted with increasing the lattice spacing and film thickness, whereas a blueshift was observed for larger lattice material refractive indices. Finally, the simulations showed some optimum



Downloaded From: https://www.spiedigitallibrary.org/journals/Journal-of-Nanophotonics on 09 May 2023
Terms of Use: https://www.spiedigitallibrary.org/terms-of-use

parameters for the development of sensors. A multilayer structure with 10 $\mu$m of thickness and a refractive contrast of around 10% showed suitability to not compromise the diffracted intensity, wavelength selectivity, or spectral peak. The parallel processing framework presented here will enable deeper insight into the diffraction process of multilayer crystal structures recorded in thick films with realistic parameters. This framework will be supportive in the development of nanostructured photonic devices for laser, sensors, and holographic materials.

## Acknowledgments

This work received funding from the European Union's Horizon 2020 research and innovation programme under the Marie Sklodowska-Curie Grant No. 896410. Also, this work has been supported by the Engineering and Physical Sciences Research Council (EP/T013567/1).

## References

1. A. Othonos et al., "Fibre Bragg gratings," in *Wavelength Filters in Fibre Optics*, H. Venghaus, Ed., pp. 189–269, Springer, Berlin, Heidelberg (2006).
2. Z. Li et al., "Multicolor photonic pigments for rotation-asymmetric mechanochromic devices," *Adv. Mater.* **34**(4), 2107398 (2022).
3. T. Ali et al., "Developing flexible liquid crystal defect mode lasers," *Proc. SPIE* **11303**, 105–117 (2020).
4. H. Kim et al., "Multifunctional photonic nanomaterials for diagnostic, therapeutic, and theranostic applications," *Adv. Mater.* **30**(10), 1701460 (2018).
5. C. P. Tsangarides et al., "Computational modelling and characterisation of nanoparticle-based tuneable photonic crystal sensors," *RSC Adv.* **4**(21), 10454–10461 (2014).
6. M. Elsherif et al., "Wearable contact lens biosensors for continuous glucose monitoring using smartphones," *ACS Nano* **12**(6), 5452–5462 (2018).
7. Y. Montelongo et al., "Reconfigurable optical assembly of nanostructures," *Nat. Commun.* **7**(1), 12002 (2016).
8. A. K. Yetisen et al., "Holographic sensors: three-dimensional analyte-sensitive nanostructures and their applications," *Chem. Rev.* **114**(20), 10654–10696 (2014).
9. A. K. Yetisen et al., "Photonic hydrogel sensors," *Biotechnol. Adv.* **34**(3), 250–271 (2016).
10. N. Jiang et al., "Doubly photopolymerized holographic sensors," *ACS Sens.* **6**(3), 915–924 (2021).
11. A. K. Yetisen et al., "Reusable, robust, and accurate laser-generated photonic nanosensor," *Nano Lett.* **14**(6), 3587–3593 (2014).
12. A. K. Yetisen et al., "Light-directed writing of chemically tunable narrow-band holographic sensors," *Adv. Opt. Mater.* **2**(3), 250–254 (2014).
13. Y. Zeng et al., "Extended plane-wave-based transfer-matrix approach to simulating dispersive photonic crystals," *Solid State Commun.* **139**(7), 328–333 (2006).
14. G. Meunier, *The Finite Element Method for Electromagnetic Modeling*, John Wiley & Sons (2010).
15. K. Yee, "Numerical solution of initial boundary value problems involving Maxwell's equations in isotropic media," *IEEE Trans. Antennas Propag.* **14**(3), 302–307 (1966).
16. U. Hohenester and A. Trügler, "MNPBEM: a Matlab toolbox for the simulation of plasmonic nanoparticles," *Comput. Phys. Commun.* **183**(2), 370–381 (2012).
17. A. K. Yetisen et al., "Mechanism of multiple grating formation in high-energy recording of holographic sensors," *Appl. Phys. Lett.* **105**(26), 261106 (2014).
18. S. Guo and S. Albin, "Simple plane wave implementation for photonic crystal calculations," *Opt. Express* **11**(2), 167–175 (2003).
19. A. Breuer-Weil et al., "Parametric simulations of slanted 1D photonic crystal sensors," *Nanosc. Res. Lett.* **11**(1), 157 (2016).
20. S. Li et al., "A MLP based FDTD method," *J. Comput. Commun.* **8**(12), 12 (2020).
21. L. Guo et al., "Study on a recurrent convolutional neural network based FDTD method," in *Int. Appl. Comput. Electromagn. Soc. Symp., China (ACES)*, vol. **1**, pp. 1–2 (2019).



Downloaded From: https://www.spiedigitallibrary.org/journals/Journal-of-Nanophotonics on 09 May 2023
Terms of Use: https://www.spiedigitallibrary.org/terms-of-use

22. H. M. Yao and L. Jiang, "Machine-learning-based PML for the FDTD method," *IEEE Antennas Wirel. Propag. Lett.* **18**(1), 192–196 (2019).
23. S. Hamedi, H. D. Jahromi, and A. Lotfiani, "Artificial intelligence-aided nanoplasmonic biosensor modeling," *Eng. Appl. Artif. Intell.* **118**, 105646 (2023).
24. S. Ohnuki et al., "Time-division parallel FDTD algorithm," *IEEE Photonics Technol. Lett.* **30**(24), 2143–2146 (2018).
25. C. Warren et al., "A CUDA-based GPU engine for gprMax: open source FDTD electromagnetic simulation software," *Comput. Phys. Commun.* **237**, 208–218 (2019).
26. S. Liu et al., "A multi-GPU accelerated parallel domain decomposition one-step leapfrog ADI-FDTD," *IEEE Antennas Wireless Propag. Lett.* **19**(5), 816–820 (2020).
27. J. Baxter, A. C. Lesina, and L. Ramunno, "Parallel FDTD modeling of nonlocality in plasmonics," *IEEE Trans. Antennas Propag.* **69**(7), 3982–3994 (2021).
28. D. Lee, T. Kim, and Q.-H. Park, "Performance analysis of parallelized PSTD-FDTD method for large-scale electromagnetic simulation," *Comput. Phys. Commun.* **259**, 107631 (2021).
29. K. Taki, "A simplified 2D numerical simulation of photopolymerization kinetics and oxygen diffusion–reaction for the continuous liquid interface production (CLIP) system," *Polymers* **12**(4), 875 (2020).
30. S. Westbeek et al., "Multiphysical modeling of the photopolymerization process for additive manufacturing of ceramics," *Eur. J. Mech.: A Solids* **71**, 210–223 (2018).
31. S. Sarkar and S. Lin-Gibson, "Computational design of photocured polymers using stochastic reaction–diffusion simulation," *Adv. Theory Simul.* **1**(7), 1800028 (2018).
32. C. E. Shannon, "Communication in the presence of noise," *Proc. IRE* **37**(1), 10–21 (1949).
33. T. Erdogan, "Fiber grating spectra," *J. Light. Technol.* **15**(8), 1277–1294 (1997).
34. G. Beadie et al., "Refractive index measurements of poly(methyl methacrylate) (PMMA) from 0.4–1.6 $\mu$m," *Appl. Opt.* **54**(31), F139–F143 (2015).



Downloaded From: https://www.spiedigitallibrary.org/journals/Journal-of-Nanophotonics on 09 May 2023
Terms of Use: https://www.spiedigitallibrary.org/terms-of-use